

Analysis of Geological Multi-Hazards in an Urban District

Cristina Di Salvo ^{1,*}, Giancarlo Ciotoli ^{1,2} , Marco Mancini ¹, Stefania Nisio ³ and Francesco Stigliano ¹

¹ National Research Council, Institute of Environmental Geology and Geoengineering (CNR-IGAG), Area Della Ricerca di Roma 1, Via Salaria Km 29,300-C.P. 10, Monterotondo Stazione, 00015 Rome, Italy; giancarlo.ciotoli@cnr.it (G.C.); marco.mancini@cnr.it (M.M.); francescopio.stigliano@cnr.it (F.S.)

² Istituto Nazionale di Geofisica e Vulcanologia (INGV), Via di Vigna Murata 605, 00143 Rome, Italy

³ Institute for Environmental Protection and Research (ISPRA), Via V. Brancati, 48, 00144 Rome, Italy; stefania.nisio@isprambiente.it

* Correspondence: cristina.disalvo@cnr.it; Tel.: +39-06-9067-2030

Abstract: This work aims to describe, classify, and analyze the occurrence of selected natural multi-hazards, specifically pluvial floods and sinkholes, affecting a district in the urban area of Rome, Italy. The procedure is based on a robust geological, geomorphological, and hydrogeological analysis performed using data collected and archived for the scope. The susceptibility is calculated based on geo-hydrological and geomorphological factors, as well as the occurrence of flooding and sinkholes. The areas prone to each single hazard were combined and put into the context of multi-hazard assessment by overlaying the susceptibility with buildings and population data. The resulting map shows that 50% of buildings (6215 inhabitants) are in an area of multi-hazard susceptibility; among these, 25% are in the highest multi-hazard classes (4 and 5). These areas are named “multi-hazard hotspots” because they are affected by many hazards with associated higher impacts. This study demonstrates that a comprehensive approach that combines the examination of geology, hydrogeology, modifications to historical morphology, and the occurrence of geological disasters is effective for mapping geohazards in urban areas and identifying locations with multiple hazards. A multi-hazard hotspot map can be used as a tool for planning actions aimed at reducing the vulnerability and exposure level of the urban population.

Keywords: geology; Rome; pluvial flood; anthropogenic sinkhole; multi-hazard



Citation: Di Salvo, C.; Ciotoli, G.; Mancini, M.; Nisio, S.; Stigliano, F. Analysis of Geological Multi-Hazards in an Urban District. *Geosciences* **2024**, *14*, 27. <https://doi.org/10.3390/geosciences14020027>

Academic Editors: Deodato Tapete and Jesus Martinez-Frias

Received: 5 December 2023

Revised: 18 January 2024

Accepted: 22 January 2024

Published: 24 January 2024



Copyright: © 2024 by the authors. Licensee MDPI, Basel, Switzerland. This article is an open access article distributed under the terms and conditions of the Creative Commons Attribution (CC BY) license (<https://creativecommons.org/licenses/by/4.0/>).

1. Introduction

Urban areas with more than 500,000 inhabitants are frequently exposed to a variety of natural hazards, such as river and pluvial floods, landslides, sinkholes, earthquakes, and land subsidence [1]. The United Nations estimated that by 2030, 60% of people worldwide, human activities, and infrastructure will be concentrated in megacities, and by 2050, this percentage will reach 68% [1]. As a result, the threat to human life and economic losses caused by natural hazards is progressively increasing, and future expectations due to urbanization and climate change predict worsening risks in the coming decades [2,3]. It is estimated that global warming will continue to increase in the near term (2021–2040), mainly due to increased cumulative CO₂ emissions in nearly all considered scenarios and pathways [4]. In the near term, every region in the world is projected to face further increases in climate hazards, increasing multiple risks to ecosystems and humans. Concurrent and repeated climate hazards will increase the impacts and risks to health, ecosystems, infrastructure, livelihoods, and food. Multiple risks interact, generating new sources of vulnerability to climate hazards and compounding overall risk. Compounding climate hazards can overwhelm adaptive capacity and substantially increase damage.

The number of disastrous events related to natural hazards is worldwide dominated by floods (occurred on average 357 times per year between 2001 and 2020), followed by storms, earthquakes, extreme temperature events, landslides, wildfires, and droughts [5].

In some cases, the interaction between multiple natural hazards occurring in the same area may affect the same exposed elements and lead to an increase in their intensity or overall impact [6,7]. Therefore, assessing the susceptibility of an area to a single hazard and/or the combination of multiple hazards (multi-hazard) is crucial for taking effective mitigation measures and increasing the cities' resilience. For instance, Karatzetzou et al., 2022 [8] described a unified methodology for the development of multi-seismic-flood hazard scenarios, aimed at the risk assessment of roadway networks at a national scale for separate, combined (triggered), or subsequent hazards. Gao et al., 2022 [9], proposed a method to determine the optimal weighting scheme when superimposing multiple geological hazards in a basin-scale area, based on objective data (which combines the analytic hierarchy process (AHP) method and the frequency ratio (FR) method) rather than the subjective experience of experts, to reduce results inaccuracy. Sun et al., 2019 [10], used the AHP to zone the single-hazard susceptibility at a basin-scale and then the barrel principle to combine multi-hazards into a comprehensive map; they found that by this method, the high-susceptibility areas do not miss any high-susceptibility single-hazard areas, and at the same time, it can select a stable area for urban development.

In this context, the geological environment (or the geological environment system) is part of the natural environment [11] and can be considered a system where the geological background and processes are integrated with human survival and development [12]. The geo-environment system interacts with the natural environment system and the socio-economic systems through various exchanges of matter and energy and continues to evolve, gradually achieving stabilizing and balancing [13]. Once the intensity of human activities exceeds the automatic adjustment capability of the geo-environment system, it can inevitably lead to various geo-hazards [10]. For instance, in the case of this research, flooding can be caused by the channelling of streams; collapses can be triggered by the excavation of geological layers. In this framework, the reconstruction of detailed geology and hydrogeology constitutes a fundamental step for detecting the geo-hazard affecting an area and for further analysis of geo-hazard susceptibility.

The multi-hazard is defined by the probability of the occurrence of multiple hazards in time and space and the associated magnitude [14–18]. Unfortunately, detailed probabilistic data on the occurrence of specific hazards for a range of severity or intensity in a specific time interval are usually not available [19]. Even in the absence of detailed probabilistic data, however, it is possible to distinguish between areas of higher and lower hazard by using occurrence data, e.g., those relating to specific events that occurred in a given historical period. In this framework, the assessment of multiple hazards does not consider the time dimension. In contrast, it focuses on identifying the proneness (e.g., susceptibility) of a specific area based on its natural characteristics (such as geological and morphological features) and the frequency of the observed phenomena. The occurrence of these phenomena, in turn, can be affected by factors related to the socio-economic activity of the area, such as the level of infrastructure development and maintenance.

Mapping the spatial distribution and hazard level for a specific geological hazard and multiple hazards can be a useful tool for planning actions aimed at reducing the vulnerability and exposure level of the urban population [20].

Many studies have focused on hazard analysis in the city of Rome, some at the municipal scale [21–26], while others are site-specific, single-hazard analyses [27–32]. In particular, the susceptibility to pluvial floods and sinkholes has been explored in urban areas and in the Italian territory by many authors [33–41]. However, these natural/anthropogenic hazards have not yet been integrated into a multi-hazard assessment.

This study presents a multidisciplinary methodology for analyzing multiple hazards, such as flooding and anthropogenic sinkholes, in the San Lorenzo district of Rome that was almost destroyed by bombing during the Second World War and completely rebuilt in the following years. The approach involves conducting a preliminary geological and morphological assessment of the area to identify the factors that may contribute to these hazards.

Our suggested approach for analyzing multiple hazards uses scores to determine the ranks of flood and sinkhole susceptibility classes. The individual susceptibilities are analyzed and modeled independently, assuming they are uncorrelated. Subsequently, they are classified into five distinct categories according to predetermined thresholds for each level of susceptibility. Finally, the individual hazards are merged to calculate the total susceptibility. In addition, we assess the number of individuals who are exposed to multiple risks. The map obtained is then overlaid with the buildings, which are classified according to the occupancy rate. The identification of multi-hazard “hotspots” is based on the locations that suffer the greatest impact from the combination of flood and sinkhole susceptibility [19]. These hotspots are locations where people may be jointly at risk of experiencing both pluvial flood and sinkhole hazards.

By using the map of the multi-hazard hotspots, a thorough evaluation of the expected impacts on human life and the economy can be conducted by considering the potential effects of floods and sinkholes, such as casualties, property damage, and economic disruption [42].

2. Study Area

The San Lorenzo District (Figure 1) is in proximity to the historical center of Rome and is known for its high population density. Throughout its existence, from ancient Roman times to the present, this place has undergone a complex and cyclical process of building, damage, and subsequent reconstruction. In addition, San Lorenzo suffered extensive bombings during World War II (July 1943–March 1944) because of its proximity to industrial buildings and railway marshaling yards. These attacks resulted in almost 4000 fatalities [43,44].



Figure 1. Location of the study area. The map shows the boundaries of the San Lorenzo district (red polygon) within the city of Rome. (Map data ©2015 Google).

Since the early 1900s, the area has shown a strong preference for the manufacturing sector, particularly small-scale enterprises that emerged in the 1920s. It is visited by numerous tourists annually due to its central location and accessibility to the two main Termini and Tiburtina railway stations. The area hosts ancient buildings and important public buildings. Comprehending the location and the geological hazards that could impact the area is crucial in determining how to plan and execute mitigation strategies.

Although numerous studies have been conducted on the subsurface of Rome at various scales of analysis and with varying degrees of detail [45–47], current drilling activities have revealed new information that was not previously considered. Holocene alluvial terrains

cross the volcanic and pre-volcanic sedimentary layers [48–50]. These terrains occur in the valleys of minor streams that were not previously included in mapping studies. The presence of alluvial terrain has significant consequences for the susceptibility to geohazards.

Both pluvial floods and sinkholes occurred in the San Lorenzo district. Pluvial floods occur when rainwater accumulates on urban surfaces. The prevalence of impermeable surfaces and the reshaping of streams contribute to an increase in surface runoff, which, during severe storms, can result in the overflow of sewers and the subsequent accumulation of water on the ground's surface. Over the past two decades, Rome has suffered more than 26 storm events that resulted in significant damage to historic buildings and commercial activities, interrupted traffic flow, and, in certain instances, resulted in fatalities [21]. Recurrent pluvial floods affect the San Lorenzo area along the main Tiburtina road and in the town square in front of the Basilica San Lorenzo Fuori le Mura, one of Rome's seven principal churches, attracting thousands of pilgrims during the Jubilee.

Rome's urban area is also highly susceptible to sudden ground collapse phenomena (e.g., anthropogenic sinkholes), mainly due to the widespread presence of hypogea (such as catacombs, cavities, and abandoned quarries) beneath the urban area. The instability and subsidence of the vaults of these underground structures can propagate to the surface, resulting in abrupt collapses. Another important consideration relates to erosive mechanisms in the subsoil resulting from exfiltrations and/or infiltrations caused by the disruption of the sewer system or the underground water supply network. As erosion propagates and underground voids enlarge, they can unexpectedly move forward to the surface, leading to the formation of sinkholes on the road level. In the latter scenario, the presence of severe weather events (characterized by high intensity and/or extended duration) could act as a triggering factor, particularly in metropolitan regions that are susceptible to floods [22]. The bombing during World War II in the San Lorenzo area significantly contributed to the erosion of the lithological layer above the subsurface cavities, making it easier for sinkhole formation, even in subsequent years.

3. Materials and Methods

3.1. Data Collection

In this study, we used various sources of information, including the following: (i) lines and point ground elevation from 1:5000 vector cartography [51]; (ii) direct observations of geological outcrops; (iii) consultation of geological and hydrogeological maps produced by the National Geological Cartographic Project (CARG); (iv) survey data and ground observations documented in scientific articles; (v) geological and hydrogeological data gathered by the IGAG or provided by the Municipality of Rome; (vi) data about the observed past floodings; and (vii) data about past collapses.

Furthermore, the evaluation of human-induced alterations in the study area was conducted using historical topographic maps obtained from the Italian Military Geographic Institute (e.g., map editions from the years 1873, 1876, and 1924). Consequently, information was collected about the gradual modification of the topographic landscape due to human-induced transformation processes, leading to an increase in anthropogenic sediments.

Observed floods include the following information:

- A vector layer with polygon geometry, with floods occurring between 2004 and 2007, was recorded and published by the Civil Protection of Rome municipality (Comune di Roma, Ufficio Extradipartimentale della Protezione Civile, 2008).
- Observed floods with point geometry occurred between 2001 and 2014, derived from the Fire Department, Municipal Police, and web media.

Observed collapses were obtained from the inventory (more than 4000 events from 1890 to the present) constructed by ISPRA (Italian Institute for Environmental Protection and Research) since 2010 in the framework of a project concerning the risk from anthropogenic sinkholes in the urban area of Rome (<https://www.isprambiente.gov.it/it/attivita/suolo-e-territorio/sinkholes-e-cavita-sotterranee/i-sinkholes-antropogenici>, accessed on 22 January 2024). ISPRA developed a sinkhole inventory through a multiphase approach

as follows: (1) collection of documents and reports for the retrospective analysis of sinkhole occurrences; (2) interpretation of multi-temporal aerial photographs; (3) morphological analysis based on DTM; (4) interviews with locals; and (5) geomorphological surveying and mapping.

Particular attention was devoted to the retrospective study of sinkhole events that took place during historic times. Bibliographic and archival research has been performed using newspapers and scientific articles at public institutions. In addition to the historical research, a detailed geomorphological analysis through high-resolution DTMs and aerial photographs allowed us to recognize the phenomena affecting the study area.

Collected data and studies were used firstly to reconstruct the morphological, geological, hydrogeological, and hydrological setting at the scale of the study area and then to support the further single-hazard susceptibility analysis.

3.2. Topographic Analysis

The high-resolution DTM (2×2 m) was built through the ANUDEM algorithm [52,53]. This tool interpolates ground elevation values by imposing constraints that ensure a connected drainage structure and the correct representation of ridges and streams from input contour data. The first DTM represents the actual topography and was built by using lines and point ground elevation from 1:5000 vector cartography [51]. The second DTM represents the pre-urbanization topography and was built by digitizing lines and points from 1924 topography [54,55]. The choice of cell resolution is consistent with the recommendations of cell size between 1×1 m and 5×5 m DTM resolution for urban flood analysis [56,57]. Then, the filling DTM tool available in the GIS environment was used to fill small DTM sinks (DTM processing errors) to obtain a hydrologically correct DTM.

3.3. Geological, Hydrological, and Hydrogeological Reconstruction

Reconstructing the geological setting of the San Lorenzo districts was particularly complex since human activities have masked most geological outcrops (i.e., rebuilt after the bombing of World War II). Therefore, to recreate the geological setting of the district, it was necessary to use the limited information gathered from the outcropping formations, integrated with topographic and subsurface data obtained from other sources.

The study area includes a total of 91 boreholes, with 37 acquired from bibliographic references and the remaining 54 obtained from private companies. The boreholes were drilled to depths ranging from a minimum of 8 m to a maximum of 91 m, measured as true vertical depth. All the boreholes crossed the anthropogenic layer, which has a thickness ranging from 1 to 20 m. A few boreholes have reached the geological substrate of the study area, which consists of over-consolidated clays termed the Monte Vaticano Formation (Pliocene). These clays lie at an elevation of roughly 0 m above sea level. Several boreholes have also crossed the system of tunnels excavated into the tuffaceous rocks below the anthropic layer. The data distribution across the area is non-uniform. Specifically, most of the data is concentrated in the northern part of the San Lorenzo district, while the density of data decreases in the central and southern parts.

3.4. Single-Hazard Analysis

3.4.1. Pluvial Flood Susceptibility Assessment

The procedure derives from [22], opportunely adapted for a reduced area, which means a reduced range of values for each one of the layers considered in the analysis.

The susceptibility is defined as the probability of flooding occurring in a certain area ("area prone to flooding") because of the ground morphology (e.g., presence of topographic depressions, area, and fill volume of depressions), the spatial probability density of observed floodings, and the proximity to sewerage. Excess stormwater flows and accumulates in the catchment's lowest elevation areas, which are, for this reason, particularly susceptible to flooding. However, floods can also be related to insufficient sewer capacity or poor manhole maintenance in areas that are not topographically depressed. Thus, areas

prone to flooding due to morphological features (depressions) were then coupled with observed floodings (flood observations dataset), comprising point and polygon geometry features, with the addition of sewer pipe hazard areas. Depressions and observed flooded areas constitute flood-prone areas, and their relative degree of susceptibility was assessed through elaborations performed by GIS tools. The phases of the susceptibility analysis are listed below. For further details, see [22]:

- (A) detection and selection of topographic depression from the DTM;
- (B) processing of observed floodings;
- (C) weighting depressions by the flood density;
- (D) weighting the flooded areas by fill depth;
- (E) combining a flood area fill depth grid and a weighted depression grid to obtain the susceptibility map of pluvial flood-prone areas.

A Detection and selection of topographic depression from the DTM

Topographic depressions, or ponds, are defined as areas having low bottom elevation surrounded by an edge with higher elevation (i.e., the difference between the filled DTM and the original DTM) with no downslope flow path. Depressions were detected by processing the DTM with the automated depression evaluation tool available in the GIS environment. In this work, this tool was used to derive areas where excess water accumulates in cases of overwhelming drainage systems and thus represent flood-prone areas. To exclude negligible and/or unrealistic features (DTM processing errors), depressions were selected, following previous experiences [57], based on their fill volume and fill depth. The minimum volume of 0.1 m^3 was considered the best threshold, allowing reliable error filtering for a $2 \times 2 \text{ m}$ cell DTM without losing a high percent of depression area and volume (Figure 2a).

B Processing of observed flooding

The punctual observed floods subtend a flooded area with unknown areal extent; the extent is assumed to be a function of the rainfall intensity and the terrain morphology. Using an Average Nearest Neighbor analysis [58,59], the distance of 202 m was calculated as the theoretical minimum extension of a flood in a condition of flat or gentle slope morphology for the observed floods in the database, extending through the whole city area. Thus, a circular buffer area with a radius of 202 m was considered around each point; then, the susceptibility of each cell in the buffer was assessed, considering the relative elevation concerning the point of observation.

C Weighting the depression layer by the flood density

To correctly map flood susceptibility, a weight was assigned to each depression. The weight accounts for the spatial probability density of observed floods. The spatial probability density is a function defining the distribution of observed floodings in space. The kernel density algorithm [60] was used to build a density map, representing the number of observed floodings per squared km; the density map was then standardized and transformed into a 0–1 value raster map, with higher values corresponding to higher flood density. The density map was multiplied by a binary grid, representing depressions. The resulting layer represents the grid of depressions weighted for the density of observed floods and was classified according to the quantile distribution to obtain a 5-class layer representing the weighted depressions. The higher the class number, the higher the flood potential (Figure 2b).

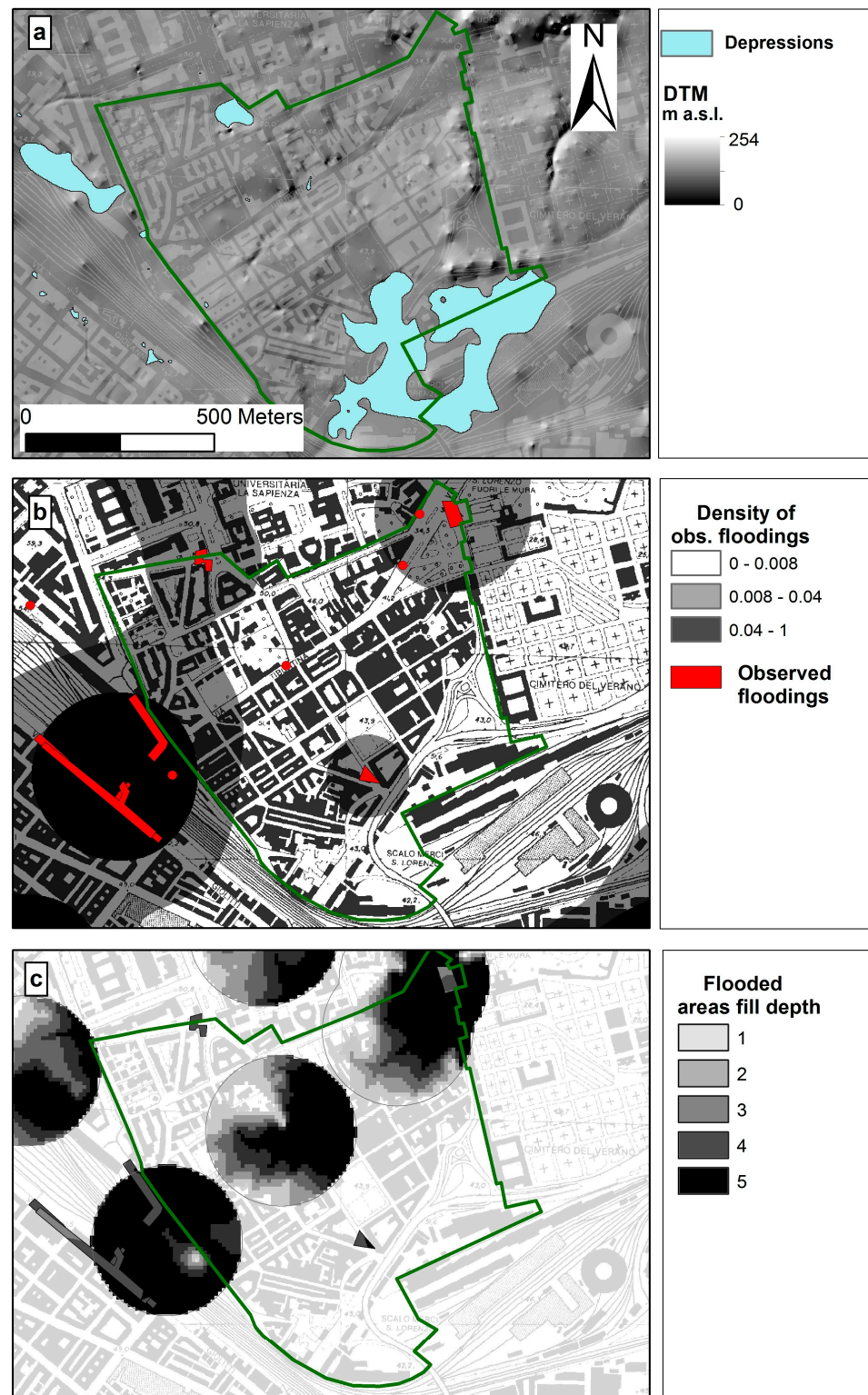


Figure 2. Reconstruction of DTM with data elaboration for the flood susceptibility analysis. (a)—topographic depression; (b)—density of observed floodings; (c)—flooded areas fill depth (for the classes, see the text). Green polygon represents the boundary of the study area.

D Weighting the flooded areas by fill depth

The threat to personal safety and gross structural damage caused by floods largely depends on the flood depth, which, in turn, depends on the rainfall intensity and the topographic characteristics of the depression. The greater the depth of the depression, the

greater the danger to people, vehicles, and goods [61]. To include the height of water filling the volume of flood-prone areas (i.e., flood depth) in the susceptibility analysis, a potential fill depth is defined, calculated in each cell as the difference between the ground elevation (DTM) and the lowest elevation of the flood-prone area in which the cell lies. For polygonal-observed floodings, the lowest elevation point coincides with the lowest elevation in the polygon. Within each of the buffered areas, the lowest elevation point is assumed to be the elevation of the punctual observed flood. Cells with fill depth ≤ 0 are considered highly susceptible, while cells with fill depth >0 are considered less susceptible because floods are expected for longer return period storms. The potential fill depth raster was categorized into 5 classes, with classes corresponding to higher susceptibility (Figure 2c):

CLASS 1: fill depth between 5 and 3 m;

CLASS 2: fill depth between 3 and 2 m;

CLASS 3: fill depth between 2 and 1 m;

CLASS 4: fill depth between 1 and 0 m;

CLASS 5: fill depth < 0 .

E Combining the fill depth grid and the weighted depression grid to obtain a map of the susceptibility to a pluvial flood

The raster maps of fill depth and of weighted depressions were summed to obtain a 10-class map of susceptibility to pluvial flooding, with higher classes corresponding to higher susceptibility. The number of classes was then reduced to five to facilitate further risk calculations.

3.4.2. Sinkhole Susceptibility Assessment

The assessment of potential hazards arising from the creation of anthropogenic sinkholes in urban areas requires a probabilistic analysis to determine the likelihood of a sinkhole event occurring within a specific timeframe. When faced with the task of developing a spatial probability model that can be extrapolated to other similar areas, a complete cartographic representation of the danger from anthropogenic sinkholes can be obtained by developing a susceptibility map that identifies areas with characteristics that favor the triggering of a sinkhole.

The conceptual model used to construct the map of sinkhole susceptibility considers the following features [37,62]:

1. The anthropogenic sinkhole occurred in the Rome area in the period 1960–2021 (a period of increased modern urban expansion) (Figure 3).
2. The identification of environmental spatial factors (recent and past) (e.g., the morphological-physiographic and geological characteristics of the Rome area) and of the anthropic aspects (e.g., the presence of underground cavities and the sewer network) that constitute the predisposing factors.
3. The application of the maximum entropy technique to derive a probabilistic model applicable in other similar areas, to provide a susceptibility map of the study area, and to evaluate the most important predisposing factors able to trigger the phenomenon. (<https://www.isprambiente.gov.it/en/archive/news-and-other-events/ispra-news/files2022/attivita/mappa-roma.jpg>, accessed on 22 January 2024. Unlike machine learning classification and regression techniques (such as the Random Forest), the application of the MaxEnt algorithm requires only the presence of event locations (e.g., Presence-only Prediction), so the response variable does not have to be a binary variable of type 0/1 (i.e., presence/absence). In this work, predictors and final susceptibility maps were re-elaborated for the San Lorenzo area according to raster maps with a 10×10 m grid.

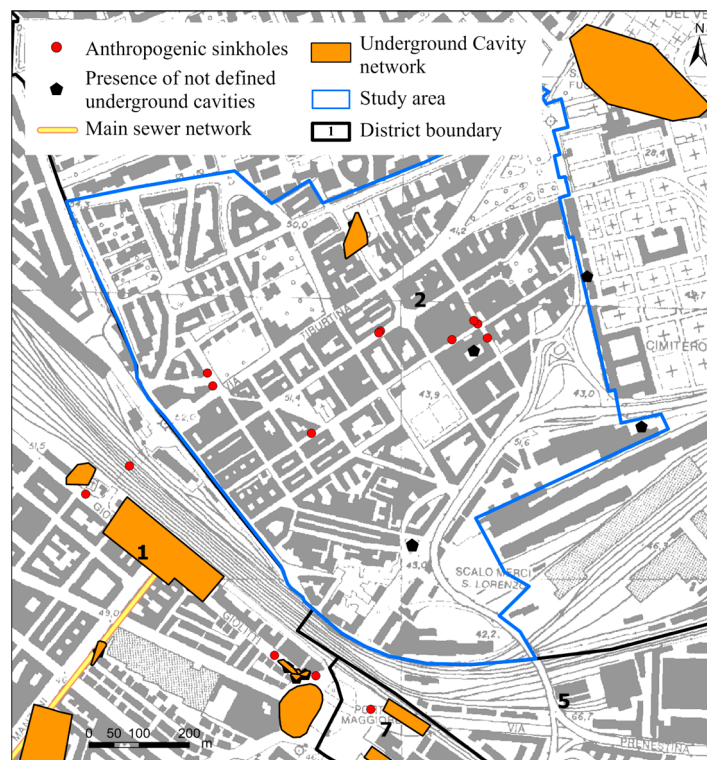


Figure 3. The location of the base factors (e.g., sinkholes, underground cavities, and main sewer network) used to construct the sinkhole susceptibility map of the San Lorenzo area. The black numbers indicate the neighbour districts.

The Presence-only Prediction method is a machine learning technique that uses the maximum entropy approach (MaxEnt) to estimate the likelihood of a phenomenon's occurrence. Unlike other methods that require the identification of absence locations, the Presence-only Prediction method uses occurrence locations and explanatory variables in the form of raster or distance features to estimate the existence of a phenomenon within the selected region of study.

In the context of maximum entropy density estimation, the real distribution of occurrences for a phenomenon is expressed as a probability distribution P across a set X of locations inside the study region. P allocates a non-negative value to each site x , and the sum of the values $P(x)$ equals one. A probability distribution model, denoted as P , is created based on a set of constraints derived from the occurrence data. For further details regarding the theoretical principles underlying the algorithm, please refer to [63,64].

Here follows a list of the conditioning and precursory factors predisposing the territory to the sinkhole phenomenon.

Anthropogenic factors.

- Sewer network (Figure 4). The location of the sewer network (provided by Roma Capitale) was included in the model as a further cause of sinkhole formation due to erosive processes of water exfiltration and infiltration due to faults, leaks, and dysfunctions of the hydraulic network, or during extreme rainfall events, which can cause surface subsidence phenomena up to the formation of sinkholes. As part of the susceptibility model, the distance between the sinkholes and the nearest collector was considered; a buffer zone of 20 m was applied to the collectors.

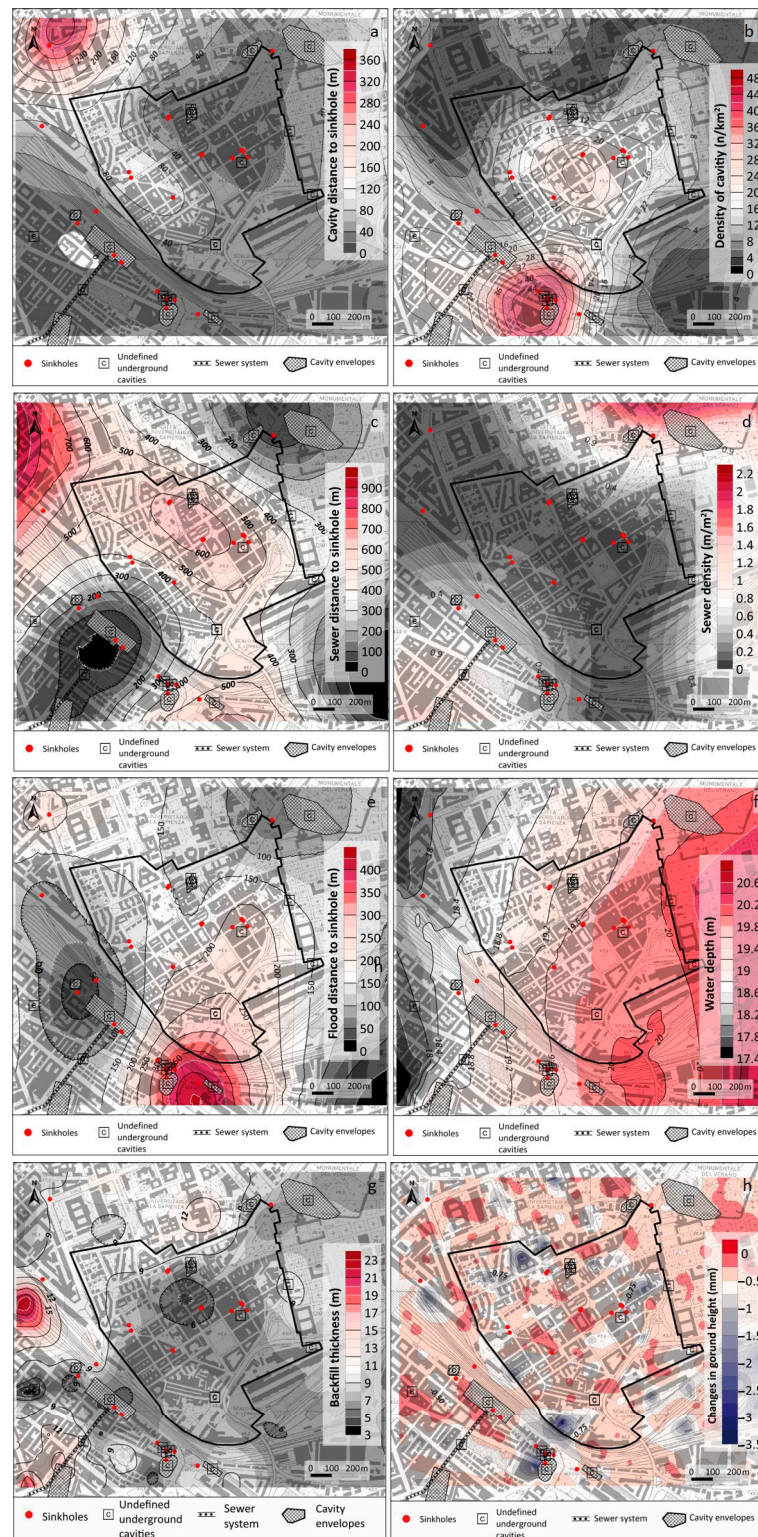


Figure 4. Maps of the conditioning and precursory factors selected to assess the sinkhole susceptibility over the Rome urban area according to a 50×50 m grid. All these factor maps were re-scaled to the San Lorenzo area and converted into continuous surface 10×10 m grids to be used as input data for the MaxEnt algorithm [37]. (a) map of the sinkhole distance from the nearest cavity; (b) map of the density of cavities; (c) map of the sinkhole distance from the nearest sewer network; (d) map of the sewer density; (e) map of the sinkhole distance from the nearest flooded area; (f) map of the depth of the water table; (g) map of the backfill thickness; (h) map of the changes in ground height from INSAR data.

- The distribution of the underground cavities reported at the ISPRA website (<https://www.isprambiente.gov.it/it/attivita/suolo-e-territorio/cartografia/carta-delle-cavita-sotterranee-di-roma> (accessed on 22 January 2024)) (Figure 4). The types of cavities that have been found in the investigated area can be classified as catacombs, single hypogea, tunnels, and bunkers [65,66]. As part of the Geographical Information System for the city of Rome, the cavities were represented in point geometry information layers, where the underground envelope of the cavity is unknown, and polygonal geometry layers, where the possibility of carrying out inspections by speleological associations allowed the reconstruction of the underground geometry of the cavity. Within the framework of the susceptibility model, the underground cavity information layers were entered in the form of a density map for point cavities and as a distance between the sinkhole and the nearest cavity.

Geological factors

- Lithology is an intrinsic predisposing factor in the urban area of Rome closely linked to the presence of underground cavities (catacombs, quarries, tunnels, etc.) that generally involve the Pleistocene pyroclastic pozzolanic and tufaceous deposits of the Albani Hills Volcanic District and, subordinately (on the hydrographic right of the Tiber), the volcanic rocks of the Sabatini Mountains Volcanic District and the Pleistocene sedimentary formations (sands and gravels of the Ponte Galeria and Santa Cecilia Units) [46,47,67–69]. The various lithologies of the litho-technical map derived from the geological map of Rome (scale 1:50,000) were grouped into 5 classes, with a score ranging from 1 to 5, based on the most quarried lithologies and the number of cavities occurring in a given lithology.
- Backfill thickness was obtained from [69] (Figure 4g). The millennia-long history of human activity in the territory of Rome has strongly reworked the topography by filling and/or obliterating river valleys, often modifying their original drainage, modifying the slopes of hillsides, building roads, extracting material from the subsoil, etc. All these activities have inevitably created a type of anthropogenic deposit known as backfill that constitutes a true “geological body” as they are constantly superimposed on the natural soil. Due to its intrinsic characteristics, the backfill is made up of very heterogeneous material with poor mechanical properties and can, therefore, be considered one of the geological factors that may condition the occurrence of sinkhole phenomena. In particular, the backfill thickness can provide important information, especially in the case of sinkholes caused by the action of fluid circulation in the subsurface [37,69]. The map of the thickness of the slopes was obtained by reprocessing the data reported in [69] with 50×50 m resolution. In the study area, the backfill thickness varies between 0 and 36 m, with a mean value of 8 m.

Morphological factors

- Satellite data (INSAR) (Figure 4h) allows the analysis of ground movements (subsidence/elevation) detected by PS (Persistent Scatterers) radar benchmarks in terms of spatial and temporal velocity patterns (mm/year). The data analysis can support the assessment of subsidence rates with millimeter accuracy over time. The analysis was performed on INSAR data provided by the Ministry of Ecological Transition (formerly the Ministry of the Environment) for the period 2005–2020. INSAR data were processed using Simple Kriging (SK) to obtain an estimated map of the subsidence velocities at a 50×50 m resolution.

Hydrogeological/hydrological factors

- Floodings distribution map (#732) is reported in [21] (Figure 4b). In the past 15 years, an increase in short-lived but heavy rainfall events (>40 mm/h) has been observed. The high susceptibility of the urban area of Rome to flooding due to heavy rainfall events is mainly due to the malfunctioning, undersized, or even absent drainage network (especially in most peripheral districts). The natural drainage network, often

obliterated, is in many areas replaced by the sewer system, which is often insufficient to support the volume of water in the event of extreme rainfall events. The stagnation of undisposed water at the surface is a factor that can increase the infiltration of water into the subsoil, resulting in the same consequences as described by the sewer collectors. The database of flooded areas in the period 2001–2014 refers to [22].

- Depth of the water table [70] (Figure 4f). In urban areas, groundwater level can condition and predispose the territory to sinkhole formation in the following cases: (i) the seasonal fluctuation of the water table level (generally lowering) can cause a loss of support for the fine material in the rocky spaces to the point of giving rise to collapse phenomena on the surface; (ii) the modification of the gradient of the water table level (due to the removal or introduction of water into the hydrogeological system) can cause a rapid washout of the loose material, causing the collapse of the surface. Piezometric data referring to the depth of the surface water table in m a.s.l. were obtained from the Hydrogeological Map of the City of Rome [70,71].

The base factors predisposing the sinkhole formation in the Rome urban area were elaborated to obtain derived maps of predictors (e.g., density and distance maps) by using neighbouring analysis (near distance tool) and density maps (Kernel Density algorithm, [58]) (Figure 4a–e). These predictors were used in the MaxEnt algorithm to obtain the final susceptibility map.

3.4.3. Multi-Hazard Assessment

The single susceptibility maps were summed up to the multi-hazard using Map Algebra in ArcMap. The resulting map was then reclassified to obtain a 5-class map, with the highest class corresponding to the area with a higher level of combined susceptibility. The map of the overall susceptibility is then overlaid on the buildings, which are last classified into the number of populations [72] or destination use of the building [51].

4. Results

4.1. DTM Reconstruction and Map of the Anthropic Backfill

Two high-resolution DTMs were built (Figure 5): one derived from the modern topographic map and showing present-day topography, the other obtained from the 1924 map. The comparison between the two DTMs supports the analysis of the evolution of terrain morphology. The difference between the two DTMs provided a map of the anthropic backfill deposits and highlighted the detection of stream valleys hidden by urbanization.

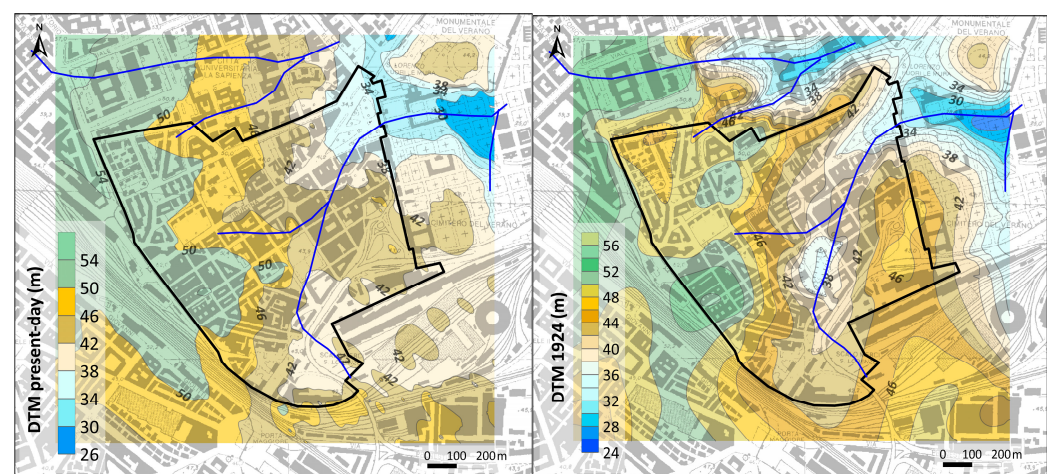


Figure 5. Reconstruction of DTM with data from present-day (left panel) and 1924 (right panel).

The map of anthropic backfill displays the main land transformations that occurred in the San Lorenzo district in the last 100 years, which correspond to: (i) removal of

natural terrains and ancient (pre-1924) anthropogenic material, featured as a negative DTM difference; (ii) accumulation of thick piles of recent anthropogenic deposits, i.e., a positive difference (Figure 6).

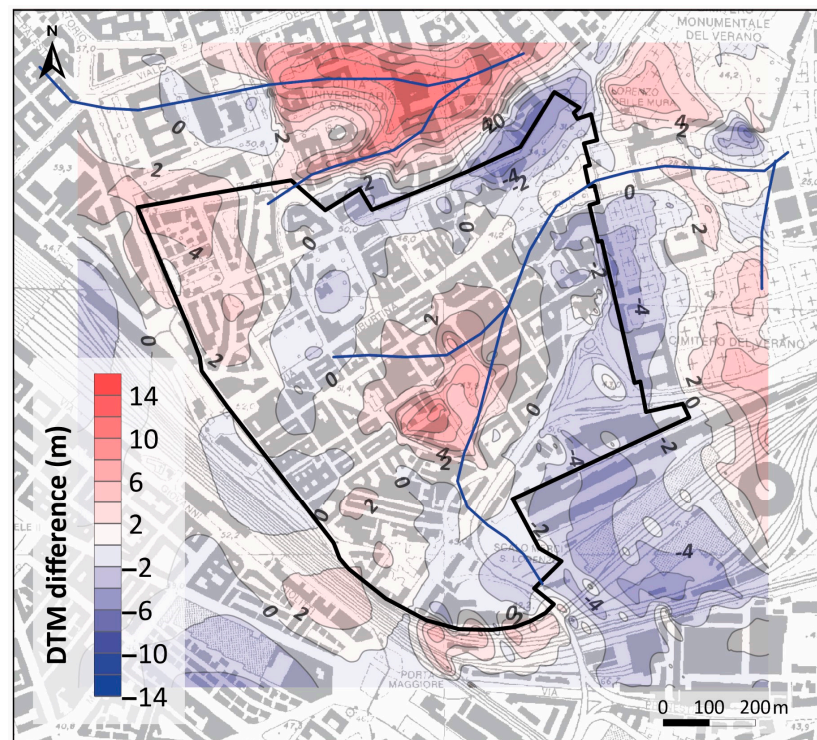


Figure 6. Difference between 1924 and present-day topographic surfaces. The green star corresponds to Piazzale del Verano; the yellow star corresponds to Sapienza University City; and the blue star corresponds to via degli Enotri.

From the map, it can be noticed that a relevant area of terrain removal is in the north-easternmost corner of the district, at Piazzale del Verano, which corresponds to the building site of “Istituto di Medicina Legale at Sapienza Università di Roma—Obitorio Comunale” (the Institute of forensic medicine of the “Sapienza” University—City Morgue). Up to the 30s’ of the past century, this site was a small natural ridge trending in the SW-NE direction [55]. In those years, the small relief was dismantled for the construction of the “Città Universitaria” (University City). Contemporary and for the same purpose, another relevant land transformation was the infilling of a large valley, almost W-E trending, with the related burying of streams, just northward of the San Lorenzo District (i.e., the large red area in the map). Here, more than 15-m-thick materials were employed to fill the ancient valley. Another relevant backfill accumulation is placed in the center of the map, filling an ancient and narrow, SW-NE trending valley (via degli Enotri site, as thick as 10 m); this site may correspond to an ancient quarry excavated in tuffs and pozzolans. In general, the very recent anthropogenic deposits have poor geotechnical properties and are prone to instabilities (settlements) and to the occurrence of polluting contaminants: metals, hydrocarbons, and plastics [73].

4.2. Geological Reconstruction

The geological sketch map in Figure 7 was obtained by a geological field survey of a few outcrops occurring in the area, coupled with the stratigraphical reconstruction of geological cross sections performed by using the available boreholes (Figure 8). The territory of San Lorenzo is part of a large plateau widening at the northwestern piedmont of the Alban Hills (Colli Albani) volcanic relief. Mean elevations are comprised of between

34 and 55 m a.s.l., which correspond to the hilltop of the plateau; lowered areas correspond to narrow valleys incised by short creeks about the modern Tiber River’s network.

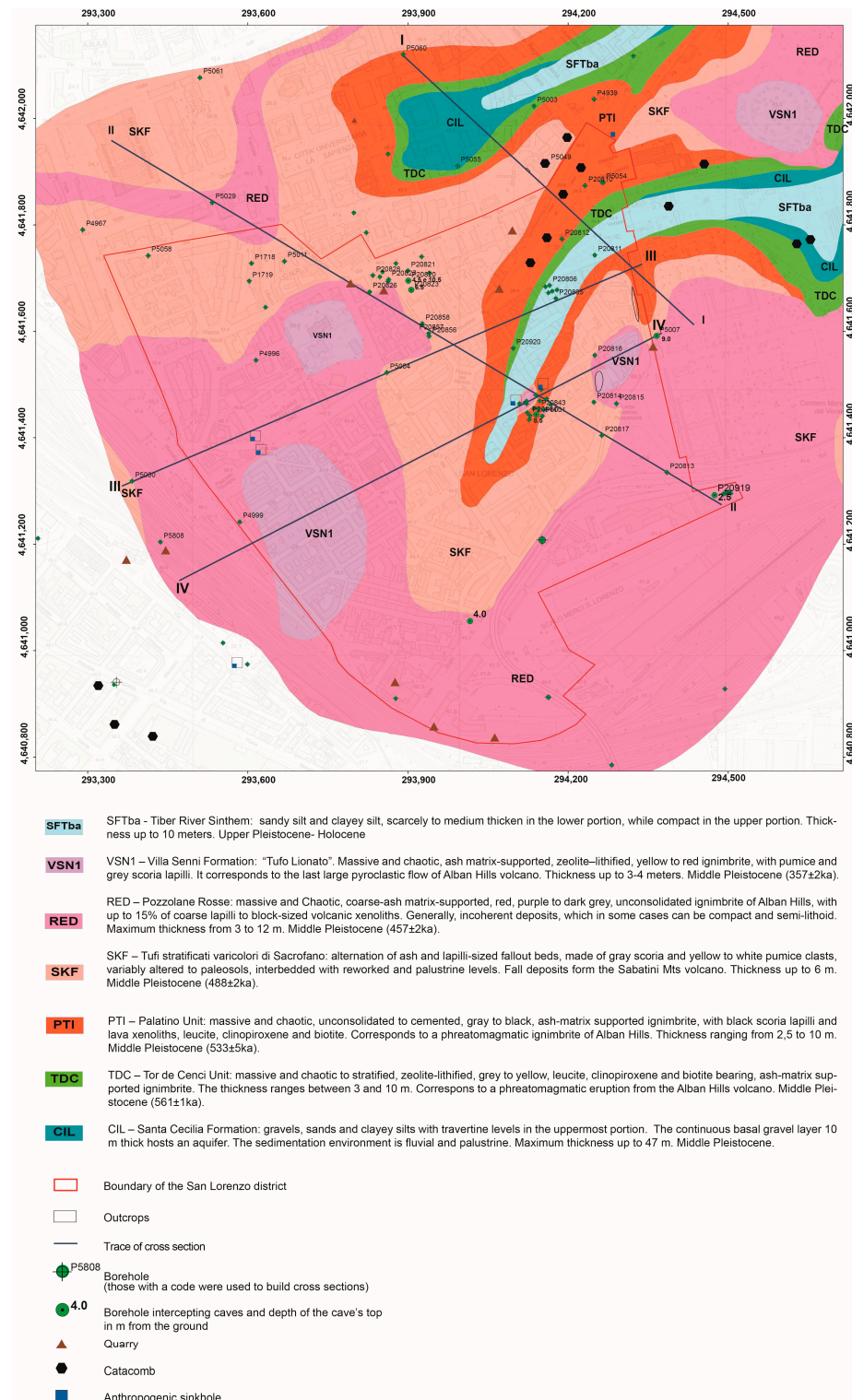


Figure 7. Geological map of the San Lorenzo neighborhood. The map shows the area of the natural geological units (i.e., the local geological substratum) present below the continuous anthropogenic cover (not shown on the map). Traces of cross sections refer to Figure 8.

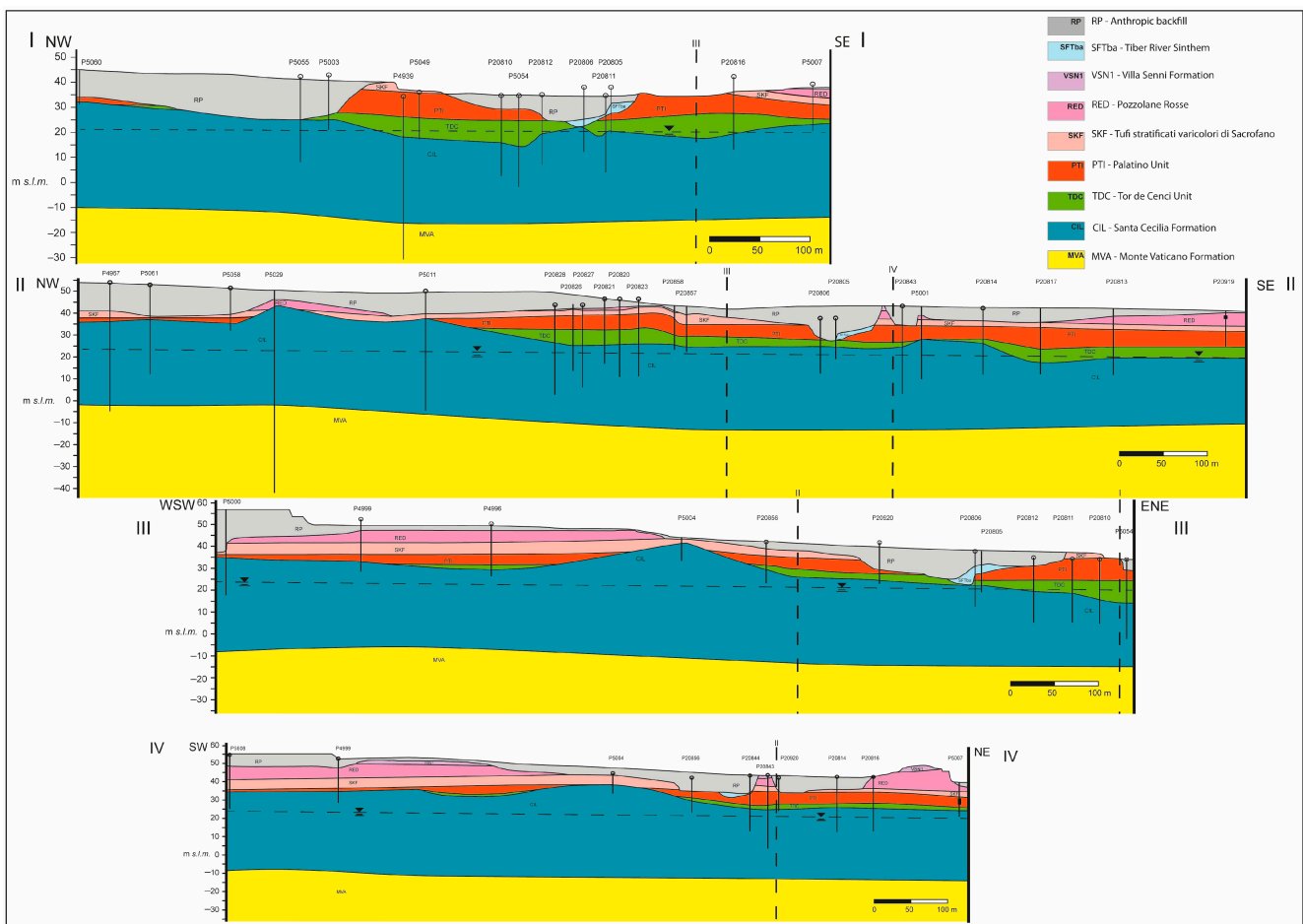


Figure 8. Cross sections (I–IV) illustrating the stratigraphic architecture of the San Lorenzo area. The geological substratum is represented by a 50-m-thick succession of middle Pleistocene sedimentary fluvio-palustrine (Santa Cecilia Formation) and pyroclastic (Tor de Cenci and Palatino Units, Tufi stratificati varicolori di Sacrofano, Pozzolane Rosse, and Villa Senni Formation) deposits overlaying the Pliocene Monte Vaticano Formation (offshore marine clays). Alluvial sediments, Holocene in age (SFTba—Tiber River Synthem) and localized in narrow paleo-valleys, and anthropogenic backfill deposits (RP) cover the middle Pleistocene sequence. The traces of sections are reported in the geological map in Figure 7.

The plateau is composed of an about 50-meter-thick multi-layered succession of sedimentary and pyroclastic deposits of the middle Pleistocene age, respectively sedimented by the ancient Tiber River system and by the Alban Hills and Sabatini Mts Volcanic Districts. The middle Pleistocene succession overlays with unconformity Pliocene marine clays of the Monte Vaticano Formation (MVA), up to 500 m thick and representing the geological bedrock in Rome [46,47] (Figures 7 and 8).

From base to top, the middle Pleistocene succession starts with the fluvial-palustrine Santa Cecilia Formation (CIL), up to 25 m in thickness and composed of gravels grading upward to sands and clay.

It follows a set of pyroclastic deposits mostly recording large-scale explosive eruptions interlayered with fall-out deposits and paleosols. At the base is the Tor de Cenci Unit (TDC), an ignimbrite that erupted at about 561 ± 1 ka [74,75], followed by the Palatino Unit (PTI), a massive old ignimbrite at 533 ± 5 ka. These basal ignimbrites, sourced by the Alban Hills volcano, are covered by the “Tufi stratificati varicolori di Sacrofano” Unit (SKF), from the Sabatini MTS Volcanic District and composed of fall-out pumices alternated with fine-grained ashes; the SKF unit is also comprised at the base of the Prima Porta ignimbrite

(not distinguished on the map). The top of the pyroclastic sequence is represented by the Pozzolane Rosse unit (RED), a non-welded ignimbrite with a coarse ashy matrix, and by the Tufo Lionato member (VSN1) of the Villa Senni formation (VSN), a massive, ignimbritic, and lithoid tuff. The RED and VSN1 units were emplaced from two large-scale eruptions from the Alban Hills and dated, respectively, 457 ± 3 ka and 357 ± 2 ka. The narrow valleys were carved in the late Pleistocene and later filled by silty-sandy alluvia of the Tiber River Synthem (SFTba; late Pleistocene–Holocene in age). The natural substratum is almost completely covered by a thick pile of anthropogenic deposits (RP), which will be better described in the following section.

4.3. Hydrology and Hydrogeology

The area is located at the boundary between two river basins (the Tiber and Aniene rivers). The hydrological divide is coincident with the western boundary of the San Lorenzo area [48] and separates streams draining easternward and westernward (Figure 9); these streams are today almost completely channelized and hidden by urbanization. In particular, the streams in the San Lorenzo area are minor tributaries of the Acqua Bullicante stream (which is, in turn, a tributary of the Aniene River), whose valley runs from south to north.

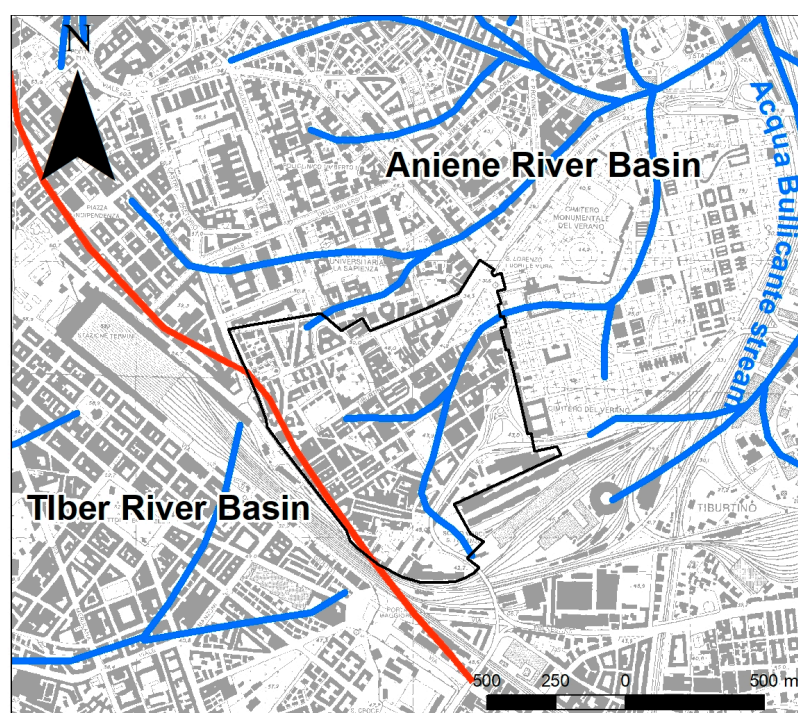


Figure 9. Streams (blue lines) and hydrological divides (red lines) [48]. The black line bounds the San Lorenzo district.

The groundwater map of Rome [70] describes a slightly different pattern of groundwater concerning surface water: a groundwater divide, NNW–SSE-oriented, runs to the east of the San Lorenzo area’s boundary. In the study area, the main groundwater direction is westward. A double groundwater circulation is detected, flowing both in the uppermost volcanic terrains (complexes VSN 1 and RED, No. 6 and No. 7 in Figure 10), with an average water table elevation of 25 m a.s.l., and in the sandy-gravelly basal layer of CIL (complex n.11 in Figure 10).

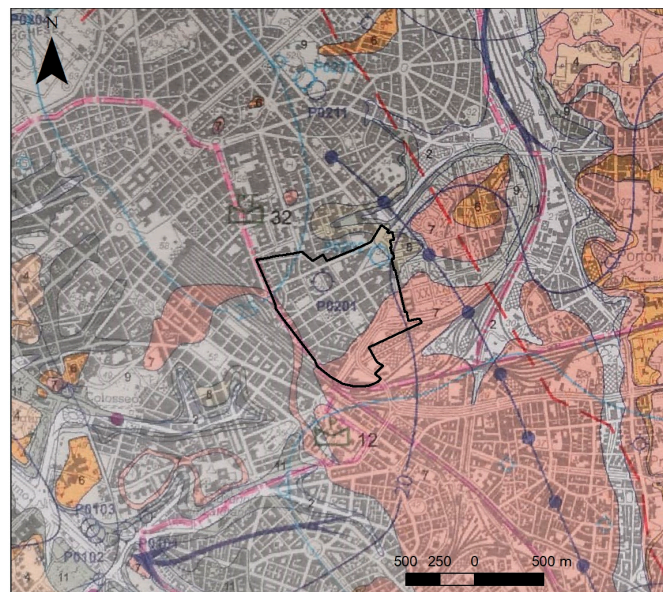


Figure 10. Hydrogeological map of the study area [70]. Hydrogeological complexes (see Table 1): 2-SFTba; 6-VSN 1; 7-RED; 8-PTI; TDC; 9-SKF; and 11-CIL. Water table and elevation in m a.s.l.: blue line (lowermost circulation) and light blue line (uppermost circulation). Blue dotted line: groundwater divide. Arrows: groundwater flow direction.

Table 1. Table lists the units, both outcropping and detected through drillings, with their thickness, age, and acronyms from the official geological map [46,47].

Unit	Acronym	Max Thickness	Age
Backfill	RP	20 m	From historical age to the actual age (about 3000 ka)
Tiber River Synthem alluvial deposit	SFTba	10 m	Upper Pleistocene pro parte—Holocene
Villa Senni Formation: Tufo Litoide Lionato	VSN1	3–4 m	Middle Pleistocene p.p. (357 ± 2 ka)
Pozzolane Rosse	RED	12 m	Middle Pleistocene p.p. (457 ± 4 ka)
Tufi stratificati varicolori di Sacrofano	SKF	6 m	Middle Pleistocene p.p. (488 ± 2 ka)
Palatino Unit	PTI	10 m	Middle Pleistocene p.p. (533 ± 5 ka)
Tor de Cenci Unit	TDC	10 m	Middle Pleistocene p.p. (561 ± 1 ka)
Santa Cecilia Formation	CIL	47 m	Middle Pleistocene p.p.
Monte Vaticano Formation	MVA	>16 m	Lower—Upper Pliocene p.p.

4.4. Map of the Susceptibility to Flood

The map of susceptibility to pluvial flooding (Figure 11) comprises five classes: 1 = very low, 2 = low, 3 = medium, 4 = high, and 5 = very high. Areas with low fill depth, a high density of observed floods, and a small fill volume belong to the ‘very high’ susceptibility class.

The San Lorenzo territory presents a susceptibility to flooding, which for 48% corresponds to very low and very high (Figure 11, left panel). This is due to the presence of relatively low areas, which are the natural destinations of waters flowing on the surface, and to observed flooding. The relatively low areas are found around the station (southeastern portion) and in the entrance area of the Verano monumental cemetery (north-east corner). The observed floods reported in the database are located along the via Tiburtina, which runs in the middle of the area from SW to NE (Figure 11, right panel), in Piazzale Aldo Moro, and in the corner between via dei Sardi and via degli Enotri. The medium class shows the highest percentage of pluvial floods (57% of susceptible surfaces, Table 2). High and very-high susceptibility zones occupy 8.8 and 0.8% of the susceptibility area, respectively.

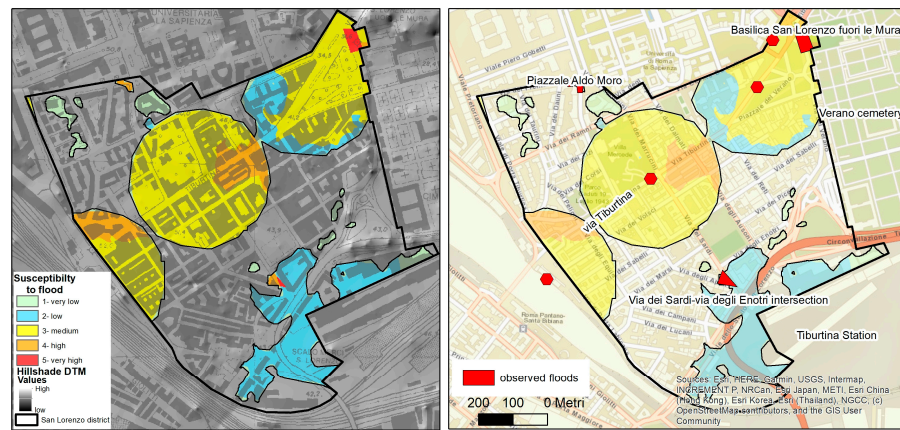


Figure 11. Susceptibility to flooding (left panel) and observed floods (right panel).

Table 2. Susceptibility classes: percentage of occurrence.

Susceptibility Class	% of Occurrence
Very low	8.4
Low	24.6
Medium	57.4
High	8.8
Very high	0.8

4.5. Map of the Susceptibility to Sinkhole

The sinkhole susceptibility map of the San Lorenzo area was obtained by extracting data from that developed for the entire urban area of Rome [37] (Figure 12). Sinkhole susceptibility values are expressed in terms of the probability of the occurrence of sinkhole events, ranging from 0 to 1. The map clearly shows that sinkhole susceptibility (above 0.6) increases in the neighboring underground cavities. The susceptibility also increases near the sewer network, as occurs in the SW corner of the map.

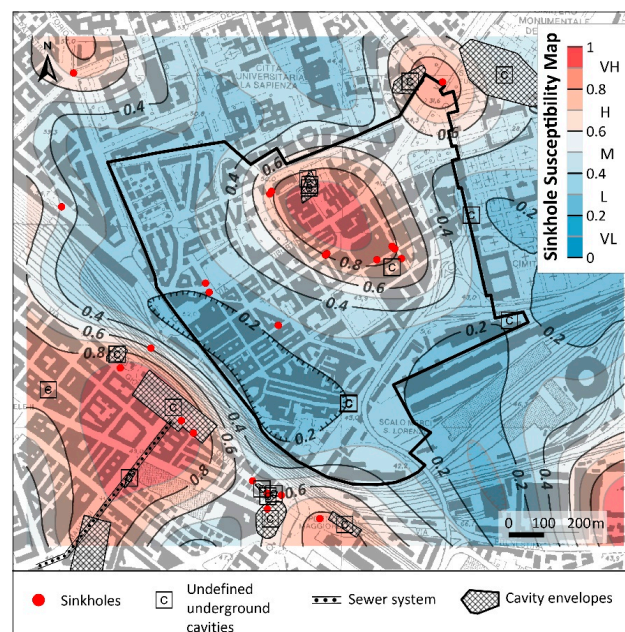


Figure 12. Map of the sinkhole susceptibility of the San Lorenzo district. Color scale: VL = very low; L = low; M = medium; H = high; and VH = very high.

The predictive capability of the sinkhole susceptibility model elaborated for the Rome urban area is very good. The ROC curve, commonly applied in machine learning techniques (including the PoP) to evaluate the model performance, provides an area under the curve of 0.850 for training data and 0.847 for test data.

The range of values of the sinkhole susceptibility map was divided into five classes by using quantiles (very low, low, medium, high, and very high). In the San Lorenzo area, 16 out of 22 sinkholes (72%) fall in areas with susceptibility greater than 0.6 (high and very high classes), while only 6 fall in susceptibility classes below 0.6 (medium, low, and very low) (28%).

4.6. Multi-Hazard Map

The multi-hazard map (Figure 13) highlights areas where the concurrence of more than one geological hazard exists. The hypothesis is that the interaction between “concurrent” hazards may lead to an increase in their intensity or overall impact; for this reason, areas with the co-existence of higher flood and sinkhole susceptibilities correspond to the higher multi-hazard classes.

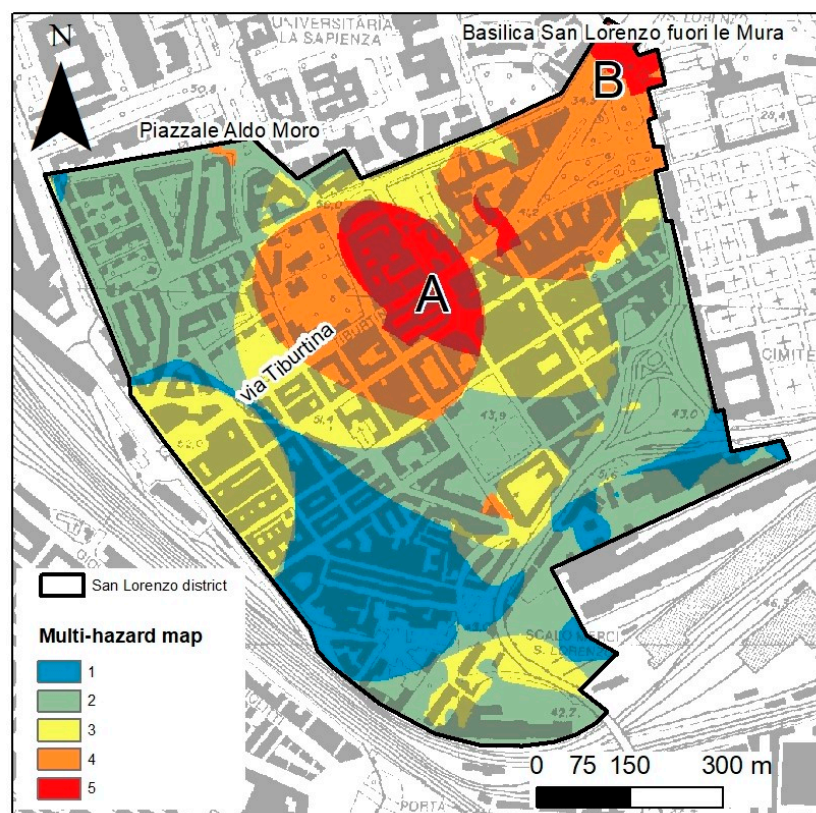


Figure 13. Multi-hazard map. The highest classes are at the crossing with via degli Ausoni (A) and in correspondence with Basilica San Lorenzo Fuori le Mura (B).

The 7% of the territory, corresponding to 47,576 m², is in the highest class of multi-hazard (5th, Figures 13 and 14): these are in three areas along Tiburtina street (the wider one at the crossing with via degli Ausoni, Figure 13(A)) and in correspondence with Basilica San Lorenzo Fuori le Mura (Figure 13(B)). Multi-hazard classes 3 and 4 represent, respectively, 42% (169,720 m²) and 37% (137,100 m²). Class 1 covers 14% of the multi-hazard map.

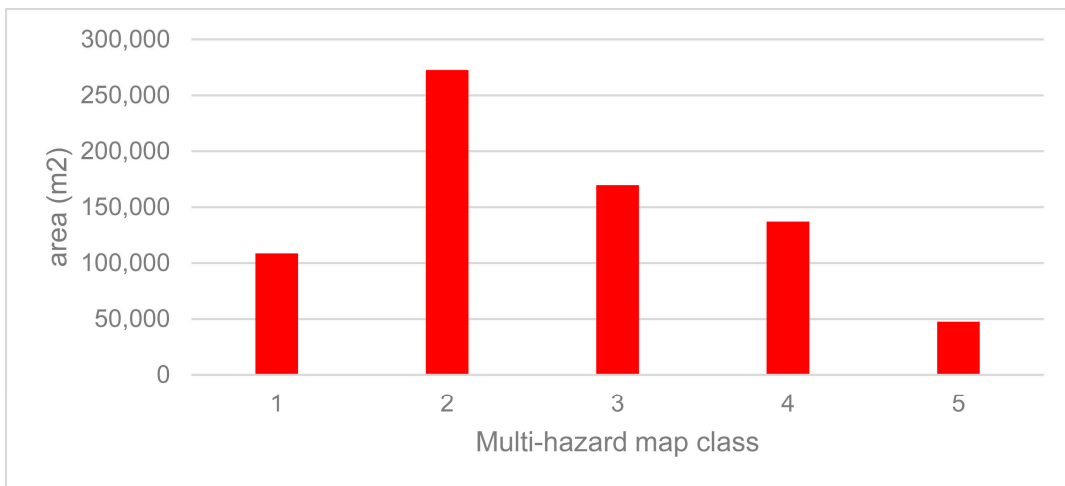


Figure 14. Histogram showing the area covered by each of multihazard class.

The overlay between the buildings and each susceptibility map (Figure 14) shows that:

- Fifty percent of buildings are in flood susceptibility areas (6215 inhabitants); between these, 34% (2770 inhabitants) are in classes high and very high.
- Hundred percent of buildings are in sinkhole susceptibility areas (9200 inhabitants); between these, 26% are in classes high and very high.

The overlay between the buildings and the multi-hazard map shows that:

- The use of buildings is mostly residential, but there are also a few industrial and railway buildings, two churches, and some shacks (Figure 15);
- Fifty percent of buildings are areas of combined susceptibility; among these, 8% are in multi-hazard class 5, and 17% are in multi-hazard class 4. In other words, 25% of buildings are in the highest multi-hazard classes (4 and 5), corresponding to about 1530 inhabitants. This area can be defined as a “multi-hazard hotspot” (Figure 16).

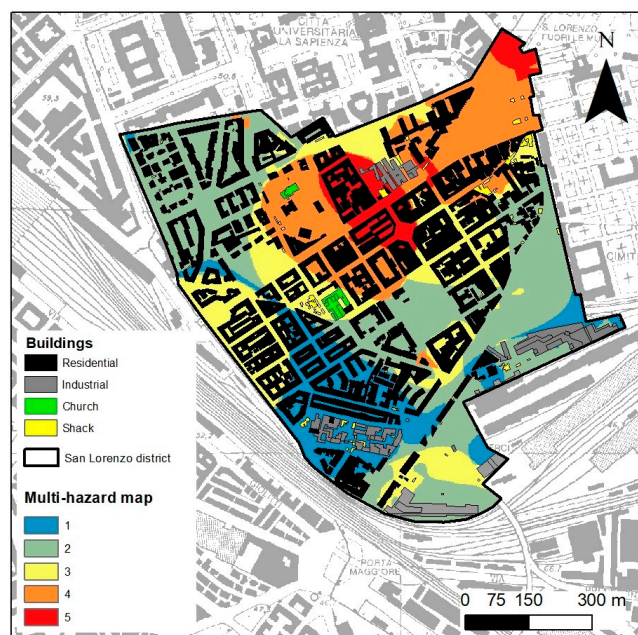


Figure 15. Buildings overlaid on the multi-hazard map.

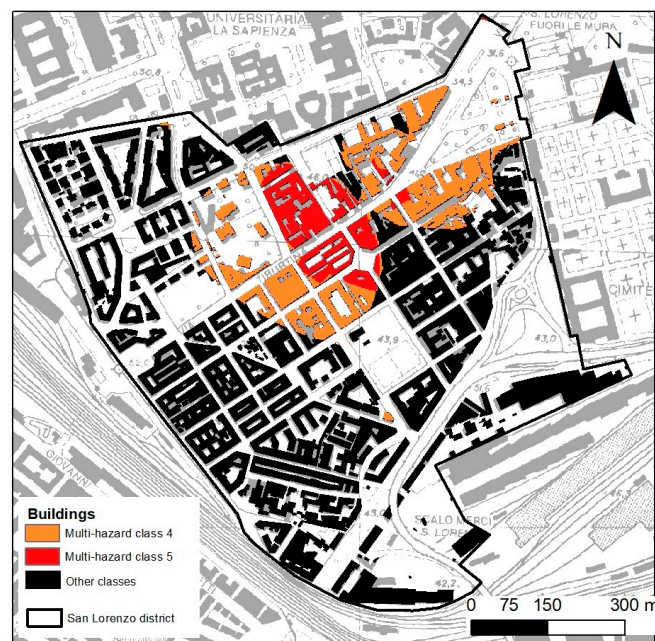


Figure 16. Map of the multi-hazard hotspots.

5. Discussion

The purpose of this work is to present a semiquantitative methodology for combining the assessment of several geohazards to which historical cities could be exposed [76–78]. The study area covered the San Lorenzo district of Rome, which suffered extensive damage from bombing during the Second World War and underwent a comprehensive reconstruction. The district, as well as the entire metropolitan area of Rome, is subject to multiple hazards, such as flooding caused by intense storms and human-induced sinkholes primarily associated with the complex system of tunnels and underground cavities.

The multidisciplinary geological, hydrological, morphological, and anthropic analyses identified several factors that predispose the San Lorenzo area to multiple geohazards (i.e., susceptibility to flooding and sinkholes). The local-scale geological map is crucial for planning actions that impact the subsoil, such as building structures or underground parking facilities [77]. The thorough geological reconstruction of the study area accurately maps the upper and lower borders of the tuff layer. During ancient Roman times, this layer experienced significant quarrying of building materials, which created an extensive network of tunnels, hypogea, and catacombs. The Roman underground environment is sometimes so extensive that it forms a city beneath the city. However, the growing urbanization since the 1950s has hidden many underground cavities, which today constitute a risk of instability and can lead to surface collapses (i.e., anthropogenic sinkholes). Results obtained from the machine learning analysis (e.g., MaxEnt algorithm) demonstrate that the existence of underground cavities significantly influences the occurrence of surface collapse. In particular, the obtained model indicates that the cavity density and sewer distance from the nearest sinkhole are the most important predictors of sinkhole susceptibility, at 44.4% and 20.1%, respectively.

The geomorphological and geological investigations, which involved the comparison between DTMs of different periods and the examination of the available boreholes' stratigraphy, enabled the reconstruction of the thickness of the backfill deposits, which can be considered a geotechnical microzonation. The map presented in Figure 6 provides an in-depth assessment of the thickness and age of anthropogenic deposits in San Lorenzo. It specifically focuses on the latest deposits resulting from local land modifications, providing an updated version of previously published maps. Areas with a greater amount of backfill material are the ones that highlight the highest level of uncertainty regarding their geotechnical properties. It is recommended to conduct supplementary surveys in

these areas, particularly when new interventions on the territory or buildings are planned. Accordingly, the map can serve as a valuable instrument for assessing geotechnical and environmental risks within the region.

This principle is additionally applicable to the assessment of anthropic risk, which encompasses the identification of explosives, contaminants, and chemicals that originated from recent industrial processes. Furthermore, due to the war bombardment, San Lorenzo may have accumulated anthropogenic deposits that could also include dangerous materials like unexploded weapons, resulting from military damage [79]. The backfill map can be used to identify the potential occurrence of not-yet-recovered and/or hidden explosives that are buried beneath recently deposited materials. The higher the thickness and recency of the deposits, the greater the likelihood of concealed explosives being present. The analysis of the current morphology also reveals the existence of relatively lower areas that serve as the natural catchments for surface water (depressions, Figure 2a). Furthermore, examining the morphology within a 200-m buffer around observed floods allows the association of the fill depth attribute with the observed floods (Figure 2c). Both depressions and fill depth are key characteristics in defining the pluvial flood susceptibility map.

As we have seen, urban environments are susceptible to various geo-hazards, which vary based on the density and composition of buildings. The vulnerability of these buildings can be assessed by analyzing the functional zoning of the area. We conducted a semi-quantitative zoning of the vulnerability of the San Lorenzo district by merging maps of pluvial floods and sinkhole susceptibility. Results of the multi-hazard analysis show that 7% of the territory is in the highest class of multi-hazard (fifth class), while multi-hazard classes 3 and 4 represent, respectively, 42% and 37% (Figure 13). Class 1 covers 14% of the multi-hazard map. Fifty percent of buildings (involving 6215 inhabitants) are in an area susceptible to flooding (Figure 15); among these, 34% (2770 inhabitants) are in classes high and very high. Moreover, all buildings are in a sinkhole susceptibility area (9200 inhabitants), with 26% in classes high and very high. Fifty percent of buildings are areas of combined susceptibility and flooding; among these, 25% (1530 inhabitants) are in the highest multi-hazard classes (4 and 5). The maximal vulnerability risk is attributed to the densely built-up territory (which is observed in residential and public zones). These areas can be defined as “multi-hazard hotspots” (Figure 16).

6. Conclusions

This study demonstrates that a comprehensive multidisciplinary approach combining the examination of urban geology and hydrogeology, historical morphology modifications, and the occurrence of geological disasters is a suitable and efficient tool for mapping geohazards in urban areas and identifying specific locations affected by multiple hazards.

The multidisciplinary approach provides the assessment of several factors (e.g., particular geological formation, backfill thickness, underground cavities, depression, fill depth, etc.) that predispose the area of San Lorenzo district to pluvial flood and sinkhole susceptibility. The semi-quantitative combination of the pluvial flood and sinkhole susceptibility maps produces a multi-hazard map that identifies areas where the occurrence of “concurrent” hazards could potentially amplify their severity or overall consequences.

The integration of the multi-hazard map with information about building type and use is a promising tool to assess the vulnerability of the urban environment and the zoning of the territory based on hazard classes. The multi-hazard hotspot map (e.g., highest multi-hazard classes) can be used to recognize areas where mitigation planning actions can be carried out. Moreover, the map can be employed to conduct a comprehensive assessment of the expected impacts on human life and the economy by considering the potential effects of floods and sinkholes, including casualties, property destruction, and economic disruption.

This study should be considered a preliminary assessment of multi-hazards at the scale of urban districts. The main limitation of this approach arises from the fact that the individual assessment of pluvial flood and sinkhole susceptibility, which was used to construct the multi-hazard map, was conducted separately using distinct quantitative

and semi-quantitative techniques. Although there may be a correlation and interdependence between both hazards (i.e., sinkhole susceptibility can increase in flood-prone areas), the incorporation of these two distinct maps necessarily introduces a certain degree of variability in our research. Nevertheless, in practical application, it can be more useful to develop a homogeneous representation of standardized hazards in order to identify multi-hazard hotspots.

Author Contributions: Conceptualization, C.D.S., G.C. and M.M.; methodology, C.D.S., G.C. and M.M.; software, F.S., G.C. and C.D.S.; validation, C.D.S. and G.C.; formal analysis, C.D.S. and G.C.; investigation, F.S. and M.M.; data curation, F.S., M.M. and S.N.; writing—original draft preparation, C.D.S., G.C., M.M. and F.S.; writing—review and editing, C.D.S.; visualization, C.D.S., G.C. and F.S.; supervision, M.M.; project administration, F.S. and M.M. All authors have read and agreed to the published version of the manuscript.

Funding: This research received no external funding.

Data Availability Statement: All data are listed within the article.

Conflicts of Interest: The authors declare no conflicts of interest.

References

1. United Nations, Department of Economic and Social Affairs, Population Division. *The World's Cities in 2018—Data Booklet*; United Nations: New York, NY, USA, 2018; (ST/ESA/SER.A/417).
2. Dottori, F.; Szewczyk, W.; Ciscar, J.C.; Zhao, F.; Alfieri, L.; Hirabayashi, Y.; Bianchi, A.; Mongelli, I.; Frieler, K.; Betts, R.A.; et al. Increased human and economic losses from river flooding with anthropogenic warming. *Nat. Clim. Change* **2018**, *8*, 1758–2678. [[CrossRef](#)]
3. Arrighi, C.; Tanganelli, M.; Cristofaro, M.T.; Cardinali, V.; Marra, A.; Castelli, F.; De Stefano, M. Multi-risk assessment in a historical city. *Nat. Hazards* **2022**, *119*, 1041–1072. [[CrossRef](#)]
4. IPCC. 2023: Sections. In *Climate Change 2023: Synthesis Report. Contribution of Working Groups I, II and III to the Sixth Assessment Report of the Intergovernmental Panel on Climate Change*; Core Writing Team, Lee, H., Romero, J., Eds.; IPCC: Geneva, Switzerland, 2023; pp. 35–115. [[CrossRef](#)]
5. CRED. *2021 Disasters in Numbers*; CRED: Brussels, Belgium, 2022; Available online: https://cred.be/sites/default/files/2021_EMDAT_report.pdf (accessed on 27 December 2023).
6. Terzi, S.; Tirresan, S.; Schneiderbauer, S.; Critto, A.; Zebisch, M.; Marcomini, A. Multi-risk assessment in mountain regions: A review of modelling approaches for climate change adaptation. *J. Environ. Manag.* **2019**, *232*, 759–771. [[CrossRef](#)] [[PubMed](#)]
7. Wang, J.; He, Z.; Weng, W. A review of the research into the relations between hazards in multi-hazard risk analysis. *Nat. Hazards* **2020**, *104*, 2003–2026. [[CrossRef](#)]
8. Karatzetzou, A.; Stefanidis, S.; Stefanidou, S.; Tsinidis, G.; Ptilakis, D. Unified hazard models for risk assessment of transportation networks in a multi-hazard environment. *Int. J. Disaster Risk Reduct.* **2022**, *75*, 102960. [[CrossRef](#)]
9. Gao, R.; Wang, C.; Liang, Z.; Han, S.; Li, B. A Research on Susceptibility Mapping of Multiple Geological Hazards in Yanzi River Basin, China. *ISPRS Int. J. Geo-Inf.* **2021**, *10*, 218. [[CrossRef](#)]
10. Sun, L.; Ma, C.; Li, Y. Multiple geo-environmental hazards susceptibility assessment: A case study in Luoning County, Henan Province, China. *Geomat. Nat. Hazards Risk* **2019**, *10*, 2009–2029. [[CrossRef](#)]
11. Wang, S.J. Interaction between human engineering activity and geo-environment and its environmental effects. *J. Geol. Hazards Environ. Preserv.* **1997**, *8*, 20–27.
12. Xu, H.L. *Environmental Geology*; Geological Publishing House: Beijing, China, 2009.
13. Huang, Y.Z. Research on the Vulnerability of the Geological Environment and Its Countermeasures in Lijiang. Ph.D. Thesis, Kunming University of Science and Technology, Kunming, China, 2010.
14. Aksha, S.K.; Resler, L.M.; Juran, L.; Carstensen, L.W. A geospatial analysis of multi-hazard risk in Dharan, Nepal. *Geomat. Nat. Hazards Risk* **2020**, *11*, 88–111. [[CrossRef](#)]
15. Tilloy, A.; Malamud, B.D.; Winter, H.; Joly-Laugel, A. A review of quantification methodologies for multi-hazard interrelationships. *Earth Sci. Rev.* **2019**, *196*, 102881. [[CrossRef](#)]
16. Goda, K.; De Risi, R. Multi-hazard loss estimation for shaking and tsunami using stochastic rupture sources. *Int. J. Disaster Risk Reduct.* **2018**, *28*, 539–554. [[CrossRef](#)]
17. Araya-Munoz, D.; Metzger, M.J.; Stuart, N.; Wilson, A.M.W.; Carvajal, D. A spatial fuzzy logic approach to urban multi-hazard impact assessment in Concepcion, Chile. *Sci. Total Environ.* **2017**, *576*, 508–519. [[CrossRef](#)] [[PubMed](#)]
18. Marzocchi, W.; Garcia-Aristizabal, A.; Gasparini, P.; Mastellone, M.L.; Di Ruocco, A. Basic principles of multi-risk assessment: A case study in Italy. *Nat. Hazards* **2012**, *62*, 551–573. [[CrossRef](#)]
19. Dille, M. *Disaster Risk Hotspots: A Project Summary*; United Nations University Press: New York, NY, USA; Tokyo, Japan, 2006; pp. 182–188.

20. Johnson, K.; Depietri, Y.; Breil, M. Multi-hazard risk assessment of two Hong Kong districts. *Int. J. Disaster Risk Reduct.* **2016**, *19*, 311–323. [[CrossRef](#)]
21. Di Salvo, C.; Ciotoli, G.; Pennica, F.; Cavinato, G.P. Pluvial flood hazard in the city of Rome (Italy). *J. Maps* **2017**, *13*, 545–553. [[CrossRef](#)]
22. Di Salvo, C.; Pennica, F.; Ciotoli, G.; Cavinato, G.P. A GIS-based procedure for preliminary mapping of pluvial flood risk at metropolitan scale. *Environ. Model. Soft.* **2018**, *107*, 64–84. [[CrossRef](#)]
23. Mastrantoni, G.; Masciulli, C.; Marinim, R.; Esposito, C.; Scarascia Mugnozza, G.; Mazzanti, P. A novel model for multi-risk ranking of buildings at city level based on open data: The test site of Rome, Italy. *Geomat. Nat. Haz. Risk* **2023**, *14*, 2275541. [[CrossRef](#)]
24. Esposito, C.; Mastrantoni, G.; Marmoni, G.M.; Antonielli, B.; Caprari, P.; Pica, A.; Schilirò, L.; Mazzanti, P.; Bozzano, F. From theory to practice: Optimization of available information for landslide hazard assessment in Rome relying on official, fragmented data sources. *Landslides* **2023**, *20*, 2055–2073. [[CrossRef](#)]
25. Delgado Blasco, J.M.; Foumelis, M.; Stewart, C.; Hooper, A. Measuring urban subsidence in the Rome metropolitan area (Italy) with Sentinel-1 SNAP-StaMPS persistent scatterer interferometry. *Remote Sens.* **2019**, *11*, 129. [[CrossRef](#)]
26. Commerci, V.; Vittori, E.; Cipolloni, C.; Di Manna, P.; Guerrieri, L.; Nisio, S.; Bertolotti, E. Geohazards monitoring in Roma from InSAR and in situ data: Outcomes of the PanGeo project. *Pure Appl. Geophys.* **2015**, *172*, 2997–3028. [[CrossRef](#)]
27. Moscatelli, M.; Mancini, M.; Stigliano, F.; Simionato, M.; Di Salvo, C.; Cavinato, G.P.; Piro, S. A multidisciplinary approach for characterizing the shallow subsoil of the Central Archaeological Area of Rome for geohazard assessment. In *Non-Intrusive Meth-odol. Large Area Urban Res*; Haynes I.P., Ravasi T., Kay S., Piro S., Liverani P., Eds.; Archaeopress Publishing Ltd.: Oxford, UK, 2023; pp. 81–86. ISBN 978-1-80327-447-8.
28. Maffucci, R.; Ciotoli, G.; Pietrosante, A.; Cavinato, G.P.; Milli, S.; Ruggiero, L.; Sciarra, A.; Bigi, S. Geological hazard assessment of the coastal area of Rome (Central Italy) from multi-source data integration. *Eng. Geol.* **2022**, *297*, 106527. [[CrossRef](#)]
29. Carapezza, M.L.; Barberi, F.; Tarchini, L.; Ranaldi, M. Hazard from endogenous gas emissions and phreatic explosions in Rome city (Italy). *Geophys. Res. Lett.* **2021**, *48*, e2020GL089797. [[CrossRef](#)]
30. Bianchi Fasani, G.; Bozzano, F.; Cardarelli, E.; Cercato, M. Underground cavity investigation within the city of Rome (Italy): A multi-disciplinary approach combining geological and geophysical data. *Eng. Geol.* **2013**, *152*, 109–121. [[CrossRef](#)]
31. Barberi, F.; Carapezza, M.L.; Ranaldi, M.; Tarchini, L. Gas blowout from shallow boreholes at Fiumicino (Rome): Induced hazard and evidence of deep CO₂ degassing on the Tyrrhenian margin of Central Italy. *J. Volc. Geother. Res.* **2007**, *165*, 17–31. [[CrossRef](#)]
32. Mancini, M.; Marini, M.; Moscatelli, M.; Pagliaroli, A.; Stigliano, F.; Di Salvo, C.; Simionato, M.; Cavinato, G.P.; Corazza, A. A physical stratigraphy model for seismic microzonation of the Central Archaeological Area of Rome (Italy). *Bull. Earthq. Eng.* **2014**, *12*, 1339–1363. [[CrossRef](#)]
33. Francipane, A.; Pumo, D.; Sinagra, M.; La Loggia, G.; Noto, L.V. A paradigm of extreme rainfall pluvial floods in complex urban areas: The flood event of 15 July 2020 in Palermo (Italy). *Nat. Hazards Earth Syst. Sci.* **2021**, *21*, 2563–2580. [[CrossRef](#)]
34. Sperotto, A.; Torresan, S.; Gallina, V.; Coppola, E.; Critto, A.; Marcomini, A. A multi-disciplinary approach to evaluate pluvial floods risk under changing climate: The case study of the municipality of Venice (Italy). *Sci. Total Environ.* **2016**, *562*, 1031–1043. [[CrossRef](#)]
35. Pacetti, T.; Cioli, S.; Castelli, G.; Bresci, E.; Pampaloni, M.; Pileggi, T.; Caporali, E. Planning Nature Based Solutions against urban pluvial flooding in heritage cities: A spatial multi criteria approach for the city of Florence (Italy). *J. Hydrol. Reg. Stud.* **2022**, *41*, 101081. [[CrossRef](#)]
36. Palla, A.; Colli, M.; Candela, A.; Aronica, G.T.; Lanza, L.G. Pluvial flooding in urban areas: The role of surface drainage efficiency. *J. Flood Risk Manag.* **2018**, *1*, S663–S676. [[CrossRef](#)]
37. Ciotoli, G.; Nisio, S. Roma città sotterranea: Storia di coltivazioni e pericolosità al dissesto. *Mem. Descr. Carta Geol. d'It.* **2023**, *110*, 145–168.
38. Bausilio, G.; Annibali Corona, M.; Di Martire, D.; Guerriero, L.; Tufano, R.; Calcaterra, D.; Di Napoli, M.; Francioni, M. Comparison of two machine learning algorithms for anthropogenic sinkhole susceptibility assessment in the city of Naples (Italy). In *Geotechnical Engineering for the Preservation of Monuments and Historic Sites III*, 1st ed.; Lancellotta, R., Viggiani, C., Flora, A., de Silva, F., Mele, L., Eds.; CRC Press: Boca Raton, FL, USA, 2022. [[CrossRef](#)]
39. Bianchini, S.; Confuorto, P.; Intriери, E.; Sbarra, P.; Di Martire, D.; Calcaterra, D.; Fanti, R. Machine learning for sinkhole risk mapping in Guidonia-Bagni di Tivoli plain (Rome), Italy. *Geocarto Int.* **2022**, *37*, 16687–16715. [[CrossRef](#)]
40. Park, J.H.; Kang, J.; Kang, J.; Mun, D. Machine-learning-based ground sink susceptibility evaluation using underground pipeline data in Korean urban area. *Sci. Rep.* **2022**, *12*, 20911. [[CrossRef](#)] [[PubMed](#)]
41. Subedi, P.; Subedi, K.; Thapa, B.; Subedi, P. Sinkhole susceptibility mapping in Marion County, Florida: Evaluation and comparison between analytical hierarchy process and logistic regression-based approaches. *Sci. Rep.* **2019**, *9*, 7140. [[CrossRef](#)] [[PubMed](#)]
42. El Morjani, Z.E.A.; Ebener, S.; Boos, J.; Abdel Ghaffar, E.; Musani, A. Modelling the spatial distribution of five natural hazards in the context of the WHO/EMRO Atlas of Disaster Risk as a step towards the reduction of the health impact related to disasters. *Int. J. Health Geogr.* **2007**, *6*, 1–28. [[CrossRef](#)] [[PubMed](#)]
43. Lytton, H.D. Bombing Policy in the Rome and Pre-Normandy Invasion Aerial Campaigns of World War II: Bridge-Bombing Strategy Vindicated and Railyard-Bombing Strategy Invalidated. *Mil. Aff.* **1983**, *47*, 53–59.

44. Giannini, M.; Massobrio, G. Bombardate l'Italia. In *Storia della Guerra di Distruzione Aerea 1940–1945*; Rizzoli Storica: Milan, Italy, 2007; p. 574.
45. Funicello, R. (Ed.) La Geologia di Roma. Il Centro Storico. In *Mem. Descr. Carta Geol. d'It.*; Servizio Geologico Nazionale: Rome, Italy, 1995; Volume 50.
46. Funicello, R.; Giordano, G. *Geological Map of Italy 1:50,000, Sheet n. 374 "Roma" and Explanatory Notes*; Servizio Geologico d'Italia, Se.l.c.a.: Firenze, Italy, 2008.
47. Funicello, R.; Giordano, G. La nuova Carta Geologica di Roma alla scala 1:10,000: Litostratigrafia e organizzazione stratigrafica. In *La Geologia di Roma. Mem. Descr. Carta Geol. d'It.*; Funicello, R., Praturlon, A., Giordano, G., Eds.; Servizio Geologico Nazionale: Rome, Italy, 2008; pp. LXXX, 39–86.
48. Luberti, G.M.; Prestininzi, A.; Esposito, C. Development of a geological model useful for the study of the natural hazards in urban environments: An example from the eastern sector of Rome (Italy). *Ital. J. Eng. Geol. Env.* **2015**, *2*, 41–62.
49. Luberti, G.M. Segnalazione dell'esistenza di un fosso nell'area di San Lorenzo e del Verano e relative implicazioni sulla carta geologica del Comune di Roma. *Prof. Geol.* **2014**, *38*, 17–21.
50. Luberti, G.M. Computation of modern anthropogenic-deposit thicknesses in urban areas: A case study in Rome, Italy. *Anthr. Rev.* **2018**, *5*, 2–27. [[CrossRef](#)]
51. Lazio, R. *Carta Tecnica Regionale Numerica, Scala 1:50,000–Provincia di Roma*; Regione Lazio: Rome, Italy, 2017.
52. Hutchinson, M.F.; Dowling, T.I. A continental hydrological assessment of a new grid-based digital elevation model of Australia. *Hydrol. Process.* **1991**, *5*, 45–58. [[CrossRef](#)]
53. ANU Fenner School of Environment and Society and Geoscience Australia. GEODATA 9 Second DEM and D8 Digital Elevation Model and Flow Direction Grid. User Guide. Geoscience Australia. 2008; p. 43. Available online: <https://ecat.ga.gov.au/geonetwork/srv/api/records/a05f7892-d78f-7506-e044-00144fdd4fa6> (accessed on 23 January 2024).
54. Piano Topografico di Roma e Suburbio (1924), scala 1:5.000, Istituto Geografico Militare, Firenze. Si Tratta di una Edizione Aggiornata e Rivisitata Rispetto a Quella Prodotta nel 1907 e pubblicata nel 1908–1909. Available online: <https://geoportale.cittametropolitanaroma.it/index.php/cartografia-storica/20/41/roma-e-suburbio-nel-1924> (accessed on 23 January 2024).
55. Frutaz, A.P. Le piante di Roma, Roma 1962, III, CCXXVII, 584. Available online: <https://geoportale.cittametropolitanaroma.it/cartografia-storica/20> (accessed on 23 January 2024).
56. Mark, O.; Weesakul, S.; Apirumanekul, C.; Boonyan Aroonnet, S.; Djordjevic, S. Potential and limitations of 1D modelling of urban flooding. *J. Hydrol.* **2004**, *299*, 284–299. [[CrossRef](#)]
57. Adeyemo, O.J.; Maksimovic, C.; Booyan–Aaronnet, S.; Leitao, J.; Butler, D.; Makropoulos, C. Sensitivity analysis of surface runoff generation for Pluvial Urban Flooding. In Proceedings of the 11th International Conference on Urban Drainage, Edinburgh, UK, 31 August–5 September 2008.
58. Hertz, P. Über den gegenseitigen durchschnittlichen Abstand von Punkten, die mit bekannter mittlerer Dichte im Raume angeordnet sind. *Math. Ann.* **1909**, *67*, 387. [[CrossRef](#)]
59. Clark, P.J.; Evans, F.C. Distance to nearest neighbor as a measure of spatial relationships in populations. *Ecology* **1954**, *35*, 445–453. [[CrossRef](#)]
60. Silverman, B.W. *Density Estimation for Statistics and Data Analysis*; Routledge: London, UK, 2018.
61. FEMA. *Guidance for Flood Hazard Analysis and Mapping*; U.S. Department of Homeland Security, 2014. Available online: https://www.fema.gov/sites/default/files/nepa/Base_Map_Guidance_May_2014_SUPERSEDED.pdf (accessed on 23 January 2024).
62. Ciotoli, G.; Corazza, A.; Finoia, M.G.; Nisio, S.; Succhiarelli, C. Gli sprofondamenti antropogenici nell'aria urbana di Roma. *Mem. Descr. Carta Geol. d'It.* **2013**, *93*, 143–182.
63. Phillips, S.J.; Anderson, R.P.; Schapire, R.E. Maximum entropy modeling of species geographic distributions. *Ecol. Model.* **2006**, *190*, 231–259. [[CrossRef](#)]
64. Phillips, S.J.; Anderson, R.P.; Dudik, M.; Schapire, R.E.; Blair, M. Opening the black box: An open-source release of Maxent. *Ecography* **2017**, *40*, 887–893. [[CrossRef](#)]
65. Nisio, S.; Allevi, A.; Ciotoli, G.; Ferri, G.; Fiore, R.; Pascucci, R.; Stranieri, I.; Succhiarelli, C. *Carta delle Cavità sotterranee di Roma*; Pubblicazione ISPRA: Rome, Italy, 2017.
66. Nisio, S.; Ciotoli, G.; Ferri, F.; Moretti, P.; Puzzilli, L.M.; Ruggiero, L.; Ruscito, V.; Carlucci, G. Primo contributo allo studio delle cavità sotterranee nascoste sotto il Parco di Centocelle nell'area urbana di Roma. *Mem. Descr. Carta Geol. d'It.* **2021**, *108*, 353–371.
67. Ventriglia, U. *Geologia della Città di Roma*; Amministrazione Provinciale di Roma: Rome, Italy, 1971; 417p.
68. Ventriglia, U. *Geologia del Territorio del Comune di Roma*; Amministrazione Provinciale di Roma: Rome, Italy, 2002; 810p.
69. Ciotoli, G.; Di Loreto, E.; Finoia, M.G.; Liperi, L.; Meloni, F.; Nisio, S.; Sericola, A. Sinkhole susceptibility map of the Lazio Region, central Italy. *J. Maps* **2016**, *12*, 287–294. [[CrossRef](#)]
70. La Vigna, F.; Mazza, R.; Amanti, M.; Di Salvo, C.; Petitta, M.; Pizzino, L.; Succhiarelli, C. Groundwater of Rome. *J. Maps* **2016**, *12*, 88–93. [[CrossRef](#)]
71. Mazza, R.; La Vigna, F.; Capelli, G.; Dimasi, M.; Mancini, M.; Mastroirillo, L. Hydrogeology of Rome. *Acque Sotterranee. Ital. J. Groundw.* **2015**, *4*, 19–30. [[CrossRef](#)]
72. ISTAT, Istituto Nazionale di Statistica. Dati Geografici e Variabili Censuarie per Sezione di Censimento, anno 2011. 2015. Available online: www.istat.it (accessed on 24 March 2017).

73. Ford, J.R.; Price, S.J.; Cooper, A.H.; Waters, C.N. An assessment of lithostratigraphy for anthropogenic deposits. In *A Stratigraphical Basis for the Anthropocene*; Waters, C.N., Zalasiewicz, J.A., Williams, M., Ellis, M.A., Snelling, A.M., Eds.; Geological Society: London, UK; Special Publications: London, UK, 2014; Volume 395, pp. 55–89.
74. Karner, D.B.; Marra, F.; Renne, P.R. The history of the Monti Sabatini and Alban Hills volcanoes: Groundwork for assessing volcanic-tectonic hazards for Rome. *J. Volc. Geother. Res.* **2001**, *107*, 185–219. [[CrossRef](#)]
75. Giordano, G. Stratigraphy, volcano tectonics and evolution of the Colli Albani volcanic field. In *The Colli Albani volcano. Special Publications of IAVCEI*; Funiello, R., Giordano, G., Eds.; Geological Society: London, UK, 2010; Volume 3, pp. 43–97.
76. Arrighi, C.; Domeneghetti, A. Brief communication: On the environmental impacts of 2023 flood in Emilia-Romagna. *Nat. Hazards Earth Syst. Sci.* **2023**, *2023*, 1–10.
77. Kozliakova, I.; Eremina, O. Mapping geological risk in urban areas. *Arab. J. Geosci.* **2020**, *13*, 492. [[CrossRef](#)]
78. Grünthal, G.; Thieken, A.H.; Schwarz, J.; Radtke, K.S.; Smolka, A.; Merz, B. Comparative risk assessments for the city of Cologne—storms, floods, earthquakes. *Nat. Hazards* **2006**, *38*, 21–44. [[CrossRef](#)]
79. Nirei, H.; Mezzano, A.; Satkunas, J.; Furuno, K.; Marker, B.; Mitamura, M. Environmental problems associated with man-made strata and their potential management. *Episodes* **2014**, *37*, 33–40. [[CrossRef](#)]

Disclaimer/Publisher’s Note: The statements, opinions and data contained in all publications are solely those of the individual author(s) and contributor(s) and not of MDPI and/or the editor(s). MDPI and/or the editor(s) disclaim responsibility for any injury to people or property resulting from any ideas, methods, instructions or products referred to in the content.